

1 **Prolonged and extended impacts of SARS-CoV-2 on the olfactory neurocircuit**

2

3 Megumi Kishimoto-Urata^{1,3}, Shinji Urata^{2,3}, Ryoji Kagoya³, Fumiaki Imamura⁴, Shin Nagayama⁵,
4 Rachel A. Reyna¹, Junki Maruyama¹, Tatsuya Yamasoba³, Kenji Kondo^{3*}, Sanae Hasegawa-Ishii^{6*},
5 Slobodan Paessler^{2*}

6

7 ¹Department of Pathology, University of Texas Medical Branch, Galveston, Texas, USA

8 ²Department of Otolaryngology, University of Texas Medical Branch, Galveston, Texas, USA

9 ³Department of Otolaryngology, Graduate School of Medicine, the University of Tokyo, Tokyo, Japan

10 ⁴Department of Pharmacology, Penn State College of Medicine, Hershey, Pennsylvania, USA

11 ⁵Department of Neurobiology and Anatomy, McGovern Medical School at the University of Texas
12 Health Science Center at Houston, Texas, USA

13 ⁶Pathology Research Team, Kyorin University, Tokyo, Japan

14

15 These authors contributed equally: Megumi Kishimoto-Urata, Shinji Urata

16 *Correspondence: kondok-tky@umin.ac.jp, sanae_ishii@ks.kyorin-u.ac.jp, slpaessl@utmb.edu

17 **Abstract**

18 The impact of SARS-CoV-2 on the olfactory pathway was studied over several time points using
19 Syrian golden hamsters. We found an incomplete recovery of the olfactory sensory neurons,
20 prolonged activation of glial cells in the olfactory bulb, and a decrease in the density of dendritic
21 spines within the hippocampus. These data may be useful for elucidating the mechanism underlying
22 long-lasting olfactory dysfunction and cognitive impairment as a post-acute COVID-19 syndrome.

23 **Results and Discussion**

24 Severe acute respiratory syndrome coronavirus 2 (SARS-CoV-2) has infected over 215 million
25 people, producing an average lethality of 2.1% worldwide¹. Olfactory dysfunction is one of the first
26 and most common symptoms of the coronavirus disease-2019 (COVID-19)². The proposed
27 mechanism underlying this SARS-CoV-2-induced olfactory dysfunction involves severe damage and
28 impairment of the olfactory epithelium (OE); previous data using animal models indicates apoptosis
29 and desquamation of the entire OE, including olfactory sensory neurons (OSNs)³. While the
30 damaged OE is gradually restored in the animal study⁴, many COVID-19 survivors clinically continue
31 to suffer from central nervous system (CNS) symptoms such as depression and memory impairment,
32 as well as chronic olfactory dysfunction in some cases⁵. This study examined the effects of SARS-
33 CoV-2 infection on the CNS using the Syrian golden hamster model, which is a well-established
34 model of COVID-19 that reproduces certain features of human disease⁶.

35 Olfactory nasal cavity has a complicated structure, divided into multiple regions, e.g. medial/lateral
36 recess on the medial-lateral axis, zone 1-4 areas on the dorsomedial-ventrolateral axis⁷. Each region
37 has a different vulnerability to external harmful agents; dorsomedial side is more vulnerable to
38 methimazole⁸, and lateral side is to lipopolysaccharide⁹. Therefore, we first analyzed the local impact
39 of SARS-CoV-2 on the OE tentatively divided into 4 regions: dorsomedial (DM), dorsolateral (DL),
40 ventromedial (VM), and ventrolateral (VL) region (**Figure 1A**). The hamsters were intranasally
41 inoculated with SARS-CoV-2 at six-weeks of age and samples were collected at several time points.
42 Using immunofluorescence, we detected a significant number of SARS-CoV-2-positive regions
43 throughout the OE at 2 days post-infection (dpi), but not at 8 dpi (**Figure 1A**). Interestingly, SARS-
44 CoV-2-infected cells were observed not only superficially but also deep within portions of the DM
45 region, including the lamina propria. The SARS-CoV-2 antigen was not observed in mature OSNs,
46 as identified by olfactory marker protein (OMP) expression, but in cells around the OSNs, mostly
47 supporting cells (SCs) (**Figure 1B**), which are known to express angiotensin converting enzyme 2
48 (ACE2), the receptor for SARS-CoV-2¹⁰. The numbers of SCs significantly decreased in the VM and

49 VL and could not be determined in the DM due to the complete loss of the OE at 5 dpi, although the
50 damage was recovered almost completely in all regions by 21 dpi (**Figure 1C**). Interestingly, no
51 SARS-CoV-2 antigen was detected within the sagittal section of the whole brain (**Figure 1-figure**
52 **supplement 1A**), including the olfactory bulb (OB, **Figure 1-figure supplement 1B**) and
53 hippocampus (**Figure 1-figure supplement 1C**). The data from our study suggest that the SARS-
54 CoV-2 did not infect the brain parenchyma or that the level of infection was below detection limit,
55 however, previous research revealed that SARS-CoV-2 RNA and viral antigen can be detected in
56 the brain¹¹. Moreover, we found that the OE thickness transiently decreased at 5 dpi but recovered
57 fully by 21 dpi, as was the case for the SC numbers (**Figure 1**, **Figure 2-figure supplement 1A,B**).
58 Nevertheless, the density of mature OSNs did not completely recover up to 42 dpi, suggesting that
59 the maturation of OSNs may be delayed and/or incomplete (**Figure 2-figure supplement 1A,C**).

60 Our data indicate that the DM is the most vulnerable to SARS-CoV-2 in the OE. This is reasonable,
61 as ACE2 receptors are predominantly expressed in this region¹². The DM is considered to be
62 included in the zone 1 of the zonal categorization⁷. Interestingly, the OSNs in zone 1 only express
63 the endocellular enzyme NAD(P)H quinone oxido-reductase 1 (NQO1)¹³. NQO1 acts as an
64 antioxidant but also mediates ROS generation, being involved in increasing certain forms of neuronal
65 damage after injury⁸. This led us to analyze the relationship between NQO1 expression patterns and
66 neural damage caused by SARS-CoV-2 infection. The numbers of OMP-positive cells decreased
67 after infection and were not completely restored in both NQO1-positive and -negative regions
68 (**Figure 2A,B,C**). However, the damage was more severe in NQO1-positive regions than in NQO1-
69 negative regions (**Figure 2D**). Furthermore, the presence of macrophages, which are labeled using
70 the ionized calcium binding adaptor molecule 1 (Iba1) suggest prolonged activation in the lamina
71 propria within NQO1-positive regions (**Figure 2E,F,G**). In contrast, macrophages quickly returned to
72 a normal level within NQO1-negative regions. These data suggest that NQO1-positive areas were
73 more susceptible to SARS-CoV-2 than the negative areas. These trends were also observed in the

74 next olfactory relay center, the OB, in which the OSNs have synaptic contact with multiple neurons
75 within the glomerulus (**Figure 3A,B**).

76 In the OB, the density of the OSN axon terminal of each glomerulus was significantly decreased
77 within NQO1-positive regions, but not in the NQO1-negative regions (**Figure 3C,D**). Interestingly, the
78 size of the glomeruli themselves decreased not only in NQO1-positive but also in NQO1-negative
79 regions (**Figure 3E,F**). These data indicate that SARS-CoV-2 infection impacts odor information
80 processing within the whole OB, but especially prominent in NQO1-positive regions. Next, we
81 carefully examined the effects of SARS-CoV-2 on the profile of glial activities (**Figure 4A**, **Figure 4-**
82 **figure supplemental 1A**, **Figure 5-figure supplemental 1A**) throughout the multiple layers of the OB:
83 the olfactory nerve layer (ONL) where the OSN axon shaft are densely packed, the glomerular layer
84 (GL) where the OSN axon synapse to the relay neurons, and the external plexiform layer (EPL)
85 where the projection neurons interact with the local interneurons. Remarkably, the Iba1 signal
86 peaked at 17 dpi (**Figure 4B**), in contrast to the OE, in which it peaked at 5 dpi, indicating that
87 microglia in the OB became activated more slowly than macrophages in the OE. Interestingly, the
88 ONL, occupied by OSN axons, showed significantly strong microglial activation, even at 5 dpi. This
89 indicates that the microglia in the ONL respond to the damage of the OSN axons from the OE
90 quickly and directly, and this damage would provide an indirect secondary impact on the
91 postsynaptic circuits in the GL and EPL. Consistent with the impact of SARS-CoV-2 on the OSN
92 axon terminals within the OB (**Figure 3**), the impact on the NQO1-positive regions was significantly
93 stronger within the ONL at 5 dpi and within the GL at 17 dpi, as compared to that of the NQO-1-
94 negative regions (**Figure 4B,D,F**). However, the area occupied by glial fibrillary acidic protein
95 (GFAP)-expressing reactivated astrocytes was enlarged at 17 dpi within the GL (**Figure 4-figure**
96 **supplemental 1B,C,E**), although the dynamics of GFAP-positive cells were not different based on
97 NQO1 expression (**Figure 4-figure supplemental 1D,F**). This indicates that astrocyte activity is
98 strongly associated with the activity of microglia in the GL compared to that in other layers.

99 Next, we examined the impact of SARS-CoV-2 on higher brain areas, including the piriform cortex
100 (PC) and the hippocampus (**Figure 5, Figure 5-figure supplemental 1**). In the PC, which is one of
101 the olfactory cortices receiving direct inputs from the OB, GFAP-expression appeared transient in
102 the pia mater but persisted in the layer 1 of the PC up to 42 dpi (**Figure 5-figure supplemental 1B**).
103 Activated microglia/macrophages cells labeled by Iba1 within the pia mater increased in numbers at
104 5 and 17 dpi, although the Iba1-positive area was unchanged in layer 1 (**Figure 5-figure**
105 **supplemental 1C,D**). The peak of this activity was not correlated to the presence of SARS-CoV-2
106 within the nasal cavity (**Figure 1A**), indicating that glial activation in the PC may not be induced
107 directly by the virus through the olfactory pathway but by local and/or systemic inflammatory
108 responses. In fact, inflammatory cytokines are systemically elevated in both severe and non-lethal
109 COVID-19 models¹⁴. Given that ACE2 is expressed in the Bowman's glands of the lamina propria¹⁵
110 and that macrophages there were activated after SARS-CoV-2 infection (**Figure 2F,G**), the immune
111 response in the lamina propria may induce the elevation of intravascular inflammatory cytokines,
112 triggering the activation of glial cells and macrophages in the CNS. In the hippocampus, GFAP-
113 positive astrocytic endfeet were easily detectable around the blood vessels of the apical dendritic
114 region at 5, 8, 17, and 42 dpi (**Figure 5B**), as compared to those of the basal region. The peak Iba1-
115 signal in the basal region was achieved by 8 dpi, with the area being restored by 42 dpi (**Figure**
116 **5C,D**). In contrast, the Iba1-signal in the apical region remained strong until 42 dpi (**Figure 5C,D,E**).
117 These data indicate that SARS-CoV-2 infection in the nostril triggered the activation of microglia and
118 astrocytes, even in the hippocampus, and that the impacts are significantly different in individual
119 layer. Thus, an interesting question could be posed as to whether the activated microglia and
120 astrocytes could induce any changes in the neuronal circuits?

121 There are many reports that reveal glial cells induce synaptic modulation¹⁶, synaptic loss⁹, synaptic
122 plasticity¹⁷, and change of synaptic density¹⁸. These changes may be associated with dementia¹⁹.
123 Therefore, we analyzed dynamics of spine density within the hippocampus using Golgi stained brain
124 sections (**Figure 5F,G**). Basal dendritic spines in the hippocampal CA1 were extremely stable. In

125 contrast, the density of apical dendritic spines was significantly decreased at 42 dpi (**Figure 5H**) This
126 finding may be associated with the prolonged activation of microglial cells, most notably significant at
127 42 dpi (**Figure 5E**). These results suggest that intranasal inoculation of SARS-CoV-2 induces glial
128 cell activation and changes spine density within the higher brain regions, including the
129 hippocampus. Future studies should determine whether these changes impact animal behavior and
130 if so, how long it is required for recovery.

131 In summary, we report that single priming with SARS-CoV-2 resulted in long-lasting effects in
132 hamsters, not only on the OE but also within the brain regions critical for cognitive function. We
133 found drastic CNS changes including glial activation and synaptic dynamics, without any SARS-
134 CoV-2 antigen by immunostaining. Our study may be of importance for better understanding the
135 mechanism(s) driving the olfactory impairment and potentially cognitive dysfunction present in
136 COVID-19 survivors.

137

138 **References**

139 1. Johns Hopkins University and Medicine, Coronavirus Resource Center. Available from:
140 <https://coronavirus.jhu.edu>.

141 2. Gandhi, R. T., Lynch, J. B. & del Rio, C. Mild or Moderate Covid-19. *N. Engl. J. Med.* **1–9** (2020).

142 3. Ye, Q. *et al.* SARS-CoV-2 infection in the mouse olfactory system. *Cell Discov.* **7**, 1–13 (2021).

143 4. Urata, S. *et al.* Regeneration Profiles of Olfactory Epithelium after SARS-CoV-2 Infection in
144 Golden Syrian Hamsters. *ACS Chem. Neurosci.* (2021).

145 5. Kumar, S., Veldhuis, A. & Malhotra, T. Neuropsychiatric and Cognitive Sequelae of COVID-19.
146 *Front. Psychol.* **12**, 1–6 (2021).

147 6. Sia, S. F. *et al.* Pathogenesis and transmission of SARS-CoV-2 in golden hamsters. *Nature* **583**,
148 834–838 (2020).

149 7. Buck, L. & Axel, R. A novel multigene family may encode odorant receptors: a molecular basis for
150 odor recognition. *Cell* **65**, 175–187 (1991).

151 8. Tuerdi, A. *et al.* Dorsal-zone-specific reduction of sensory neuron density in the olfactory
152 epithelium following long-term exercise or caloric restriction. *Sci. Rep.* **8**, 1–16 (2018).

153 9. Hasegawa-Ishii, S., Shimada, A. & Imamura, F. Lipopolysaccharide-initiated persistent rhinitis
154 causes gliosis and synaptic loss in the olfactory bulb. *Sci. Rep.* **7**, 1–14 (2017).

155 10. Brann, D. H. *et al.* Non-neuronal expression of SARS-CoV-2 entry genes in the olfactory system
156 suggests mechanisms underlying COVID-19-associated anosmia. *Sci. Adv.* **5801**, eabc5801
157 (2020).

158 11. de Melo, G. D. *et al.* COVID-19-related anosmia is associated with viral persistence and
159 inflammation in human olfactory epithelium and brain infection in hamsters. *Sci. Transl. Med.* **13**,

160 eabf8396 (2021).

161 12. Fodoulian, L. *et al.* SARS-CoV-2 Receptors and Entry Genes Are Expressed in the Human
162 Olfactory Neuroepithelium and Brain. *iScience* **23**, (2020).

163 13. Gussing, F. & Bohm, S. NQO1 activity in the main and the accessory olfactory systems correlates
164 with the zonal topography of projection maps. *Eur. J. Neurosci.* **19**, 2511–2518 (2004).

165 14. Jiao, L. *et al.* The olfactory route is a potential way for SARS-CoV-2 to invade the central nervous
166 system of rhesus monkeys. *Signal Transduct. Target. Ther.* **6**, 169 (2021).

167 15. Chen, M. *et al.* Elevated ACE-2 expression in the olfactory neuroepithelium: Implications for
168 anosmia and upper respiratory SARS-CoV-2 entry and replication. *Eur. Respir. J.* **56**, (2020).

169 16. Schafer, D. P. *et al.* Microglia Sculpt Postnatal Neural Circuits in an Activity and Complement-
170 Dependent Manner. *Neuron* **74**, 691–705 (2012).

171 17. Abbott, L. F. & Nelson, S. B. Synaptic plasticity: taming the beast. *Nat. Neurosci.* **3**, 1178–1183
172 (2000).

173 18. Zhan, Y. *et al.* Deficient neuron-microglia signaling results in impaired functional brain connectivity
174 and social behavior. *Nat. Neurosci.* **17**, 400–406 (2014).

175 19. Clare, R., King, V. G., Wirenfeldt, M. & Vinters, H. V. Synapse loss in dementias. *J. Neurosci. Res.*
176 **88**, 2083–2090 (2010).

177 20. Jiao, Y. *et al.* A simple and sensitive antigen retrieval method for free-floating and slide-mounted
178 tissue sections. *J. Neurosci. Methods* **93**, 149–162 (1999).

179 21. Ranjan, A. & Mallick, B. N. Differential staining of glia and neurons by modified Golgi-Cox method.
180 *J. Neurosci. Methods* **209**, 269–279 (2012).

181 22. Angulo, A., Merchan, J. A. & Molina, M. Golgi-Colonnier method: Correlation of the degree of

182 chromium reduction and pH change with quality of staining. *J. Histochem. Cytochem.* **42**, 393–403
183 (1994).

184 23. Berbel, P. J. Chromation at low temperatures improves impregnation of neurons in Golgi-aldehyde
185 methods. *J. Neurosci. Methods* **17**, 255–259 (1986).

186 24. Tokuno, H., Nakamura, Y., Kudo, M. & Kitao, Y. Effect of Triton X-100 in the Golgi-Kopsch method.
187 *J. Neurosci. Methods* **35**, 75–77 (1990).

188 25. Ranjan, A. & Mallick, B. N. A modified method for consistent and reliable Golgi-Cox staining in
189 significantly reduced time. *Front. Neurol.* **DEC**, 1–8 (2010).

190 26. Kikuta, S. *et al.* Sensory deprivation disrupts homeostatic regeneration of newly generated
191 olfactory sensory neurons after injury in adult mice. *J. Neurosci.* **35**, 2657–2673 (2015).

192 27. SMITH, O. A. J. & BODEMER, C. N. A stereotaxic atlas of the brain of the golden hamster
193 (*Mesocricetus auratus*). *J. Comp. Neurol.* **120**, 53–63 (1963).

194 28. Knafo, S., Ariav, G., Barkai, E. & Libersat, F. Olfactory learning-induced increase in spine density
195 along the apical dendrites of CA1 hippocampal neurons. *Hippocampus* **14**, 819–825 (2004).

196 29. Mitra, R., Jadhav, S., McEwen, B. S., Vyas, A. & Chattarji, S. Stress duration modulates the
197 spatiotemporal patterns of spine formation in the basolateral amygdala. *Proc. Natl. Acad. Sci. U. S.*
198 *A.* **102**, 9371–9376 (2005).

199

200 **Figure legends**

201 **Figure 1** | Distribution of severe acute respiratory syndrome coronavirus 2 (SARS-CoV-2) in the OE.

202 A, Distribution of SARS-CoV-2 in the olfactory epithelium (OE) at mock, 2 dpi, and 8 dpi. The OE
203 was divided into 4 regions: dorsomedial (DM), dorsolateral (DL), ventromedial (VM), and
204 ventrolateral (VL). SARS-CoV-2-positive cells were localized in the 4 regions of the OE at 2 dpi. The
205 white arrows indicate the SARS-CoV-2-positive cells in the lamina propria. Scale bars, 1 mm (left),
206 100 μ m (right).

207 B, Profile of SARS-CoV-2 infection in the OE. The apical white dashed line indicates the surface of
208 the epithelium. The basal white dashed line is the border of the OE and lamina propria. Scale bar, 50
209 μ m.

210 C, Numbers of the supporting cells (SCs) in the OE in DM, DL, VM, and VL. (one-way ANOVA
211 followed by Dunnett's post hoc test. * p < 0.05, ** p < 0.01, *** p < 0.001, † means unevaluable as the
212 OE was completely desquamated and SCs were not detectable). Number of samples; n = 3 (5, 21
213 and 42 dpi) and 4 (mock).

214

215 **Figure 2** | Region-specific damage of the olfactory epithelium (OE) due to SARS-CoV-2 infection.

216 A, Representative coronal section of the OE stained with olfactory marker protein (OMP), NAD(P)H
217 quinone oxido-reductase 1 (NQO1), and DAPI. The white dashed line is the border of the NQO1-
218 positive or -negative region. Scale bar, 1 mm.

219 B, Representative images of OMP-positive cells at 5, 21, and 42 dpi or mock in the OE. The white
220 dashed line is the border between the OE and lamina propria. The asterisk indicates desquamated
221 epithelium. Scale bar, 100 μ m.

222 C, Numbers of OMP-positive cells in the NQO1-positive or -negative region. (one-way ANOVA
223 followed by Dunnett's post hoc test. **p < 0.01, ***p < 0.001, † means unevaluable as the OE was
224 completely desquamated and OMP-positive cells were not countable). Number of samples: n = 3 (5,
225 21 and 42 dpi) and 4 (mock).

226 D, Comparison of the normalized density of OMP-positive cells in NQO1-positive and NQO1-
227 negative regions. (n = 3, Welch's t-test. *p < 0.05, † means unevaluable as the OE was completely
228 desquamated and OMP-positive cells were not countable).

229 E, Representative coronal section of the OE stained with ionized calcium binding adaptor molecule 1
230 (Iba1), NQO1, and DAPI. The white dashed line is the border of the NQO1-positive or -negative
231 region. Scale bar, 1 mm.

232 F, Representative images of Iba1-positive cells at 5, 17, and 42 dpi or mock. The white dashed line
233 is the border between the OE and lamina propria. Lamina propria, LP. Scale bar, 100 μ m.

234 G, Densities of Iba1-positive cells in the NQO1-positive or -negative region. (one-way ANOVA
235 followed by Dunnett's post hoc test. ***p < 0.001). Number of samples: n = 3 (5, 17 and 42 dpi) and
236 4 (mock).

237

238 **Figure 3** | Region-specific changes in the glomeruli in the olfactory bulb (OB) due to SARS-CoV-2
239 infection.

240 A, Representative coronal section of the OB stained with olfactory marker protein (OMP), NQO1,
241 and DAPI. Scale bar, 1 mm.

242 B, Representative time series of glomeruli stained with OMP. Each circled area corresponds to a
243 glomerulus. Scale bar, 100 μ m.

244 C, The density of OMP-positive areas within the glomerulus compared between NQO1-positive or -
245 negative regions. (n =3, one-way ANOVA followed by Dunnett's post hoc test. **p < 0.01, ***p <
246 0.001).

247 D, Comparison of the normalized OMP-positive area in NQO1-positive and NQO1-negative regions.
248 (n = 3, Welch's t-test. **p < 0.01).

249 E, The size of the glomerulus at 42 dpi and mock. (Welch's t-test. ***p < 0.001). Number of samples;
250 n = 78, 60, 86, and 67 glomeruli from 42 dpi of NQO1-positive, mock of NQO1-positive, 42 dpi of
251 NQO1-negative, and mock of NQO1-negative, n = 3 animals in individual group.

252 F, Histogram of the area of the glomerulus. The regression curves were fitted using kernel density
253 estimation.

254

255 **Figure 4** | Region-specific microglial activation in the OB due to SARS-CoV-2 infection.

256 A, Representative coronal section of the OB stained with Iba1, NQO1, and DAPI. The OB has a
257 multi-layered structure from surface to the center; Olfactory nerve layer (ONL), Glomerular layer (GL),
258 External plexiform layer (EPL), Mitral cell layer (MCL), Internal plexiform layer (IPL), and Granule cell
259 layer (GNL). Squares are representative regions in the analysis of NQO1-positive and -negative
260 region. Scale bar, 1 mm.

261 B, Representative images of ONL, GL, and EPL stained with Iba1, NQO1, and DAPI. White dashed
262 circles indicate glomeruli. Scale bar, 200 μ m.

263 C,E,G, Iba-1-positive area in the ONL (c), GL (e), and EPL (g). (n = 3, one-way ANOVA followed by
264 Dunnett's post hoc test. *p < 0.05, **p < 0.01, ***p < 0.001).

265 D,F,H, Comparison of the normalized values of the Iba1-positive area in NQO1-positive and NQO1-
266 negative regions in the ONL (d), GL (f), and EPL (h). (n = 3, Welch's t-test. *p < 0.05, **p < 0.01).

267

268 **Figure 5** | Glial activation and loss of dendritic spines in the hippocampus due to SARS-CoV-2
269 infection.

270 A, The upper image is a representative coronal image of the cerebral hemisphere stained with Iba1,
271 GFAP, and DAPI. The upper white square indicates the hippocampal formation (HPF). The lower
272 panel is a high-magnification image. The lower white square-labeled region (CA1) is enlarged in
273 **Figure 5B**. Scale bar, 5 mm (upper), 1 mm (lower).

274 B, Representative image of astrocytes in the CA1 stained with glial fibrillary acidic protein (GFAP)
275 and DAPI at 5, 8, 17, 42 dpi, and mock. Arrows indicate GFAP-positive astrocytic endfeet. Corpus
276 callosum, cc; Basal dendrite layer, Ba; Pyramidal cell layer, Py; Apical dendrite layer, Ap; stratum
277 lacunosum-moleculare, slm. Scale bar, 100 μ m

278 C, Representative image of microglia in the basal and apical region of the CA1 stained with Iba1.
279 Arrows indicate Iba1-positive microglia. Scale bar, 100 μ m

280 D, Area of Iba1-positive cells in the apical and basal regions of the CA1. (n = 3, one-way ANOVA
281 followed by Dunnett's post hoc test. *p < 0.05, **p < 0.01, ***p < 0.001).

282 E, Comparison of the normalized density of Iba1-positive cells in the NQO1-positive and NQO1-
283 negative regions. (n = 3, Welch's t-test. *p < 0.05, **p < 0.01).

284 F, Upper panel is a representative image depicting Golgi-impregnated neurons of the cerebral
285 hemisphere. Lower panel is a high-magnification image of the CA1. Scale bar, 100 μ m.

286 G, Representative image depicting Golgi-impregnated dendrites and dendritic spines in the apical
287 and basal region of the CA1. Scale bar, 5 μ m.

288 H, Densities of apical and basal dendritic spines. (n = 3, one-way ANOVA followed by Tukey's post
289 hoc test. *p < 0.05, **p < 0.01, neurons = 24, 48, 46; spines = 1610, 1789, 2453 from the basal
290 dendrites of 8, 42 dpi, and mock group, neurons = 25, 41, 43; spines = 1252, 1262, 1317 from the
291 apical dendrites of 8, 42 dpi and mock group) .

292 **Methods**

293 **Cell and virus**

294 Vero E6 cells were maintained using Dulbecco's modified Eagle's medium (DMEM) supplemented
295 with 10% fetal bovine serum (FBS), 1% penicillin-streptomycin, and L-glutamine. SARS-CoV-2
296 (USA/WA-1/2020) was propagated in Vero E6 cells with DMEM supplemented with 2% FBS. Cell
297 culture supernatant was stored in the -80°C freezer until use.

298

299 **Animal experiments**

300 Six-week-old female Syrian golden hamsters were purchased from Charles River. Syrian golden
301 hamsters were anesthetized with isoflurane and inoculated bilateral-intranasally with 10^5 50% tissue
302 culture infectious dose (TCID50) of SARS-CoV-2 diluted in 100 μ l of phosphate-buffered saline
303 (PBS) or PBS as a mock control. Mock controls were sacrificed 42 days after inoculation. All
304 hamsters were housed in the animal biosafety level-2 (ABSL-2) and ABSL-3 facilities within the
305 Galveston National Laboratory at the University of Texas Medical Branch (UTMB). All animal studies
306 are reviewed and approved by the Institutional Animal Care and Use Committee at UTMB and are
307 conducted according to the National Institutes of Health guidelines.

308

309 **Immunohistochemistry**

310 Hamsters were euthanized using a high-flow rate of CO₂ followed by thoracotomy at each time point
311 to collect samples. The heads of hamsters were fixed in 10% buffered formalin for 7 days before
312 removal from the BSL-3 facility and followed by incubation in phosphate buffered saline (PBS). After
313 OBs were extracted from the skull, right OBs were sectioned into 100 μ m thick sections using a
314 vibratome and left OBs were proceeded to the tissue Golgi-Cox procedures. The nasal tissues

315 including the olfactory epithelium were decalcified with 10% EDTA (pH 7.0) for 7 days at 37 °C with
316 gentle shaking. Decalcification samples were dehydrated in 100% ethanol three times and
317 embedded in paraffin. Serial coronal sections (5 µm thick) were cut and mounted on glass slides.
318 Deparaffinized sections and free-floating brain slices were incubated for 10-30 min in Target
319 Retrieval Solution (S1700; Dako) at 72-102 °C in a water-bath for antigen retrieval²⁰. Non-specific
320 antibody binding was blocked by Serum-free protein block (Dako). Samples were incubated for 12 hr
321 in a solution containing the following primary antibodies: olfactory marker protein (OMP, goat
322 polyclonal, 1:5000 dilution; Wako Chemicals), SARS-CoV-2 Nucleocapsid antibody (rabbit polyclonal,
323 1:100; Sino Biological), anti-Iba1 (rabbit polyclonal, 1:300; Wako), anti-Iba1 for paraffin section
324 (rabbit polyclonal, 1:300; Wako), anti-Iba1 (goat polyclonal, 1:300; Abcam), anti-NQO1 (rabbit
325 polyclonal, 1:300; Cell Signaling), anti-NQO1 (goat polyclonal, 1:300; Abcam), and anti-GFAP
326 antibody (mouse monoclonal, 1:500; Millipore). Unbound antibodies were removed by washing for 3
327 min with PBS or 30 min with PBS containing 0.1% Triton X-100, respectively. Primary antibodies
328 were detected by incubation for 1 hr with a solution containing the following secondary antibodies;
329 goat anti-rabbit Fluor 488, goat anti-mouse Fluor 568, donkey anti-goat Alexa Fluor 488, and donkey
330 anti-rabbit Alexa Fluor 568 (1:200; Invitrogen). To visualize cell nuclei, DAPI or Hoechst 33342
331 (1:500; Thermo Fisher) was applied during the secondary antibody stain. Samples were mounted in
332 Vectashield hard-set mounting medium (Vector Laboratories) or 70% Glycerol.

333

334 Golgi-Cox staining
335 To quantify the number of dendritic spines, brain slices were treated with the Rapid GolgiStain Kit
336 according to the manufacturer's instructions (ND Neurotechnologies, Inc., PK401) with minor
337 modifications. Since sample conditions, especially after formalin fixation, were significant and critical
338 variables for Golgi staining²¹⁻²⁴, modified Golgi-Cox staining was performed as described in previous
339 reports^{24,25}. Briefly, the brain slices were incubated in the impregnation solution for 14 days in 37°C.

340 The impregnation solution was mixed using a 1:1 ratio of Solutions A and B, which contain mercuric
341 chloride, potassium dichromate, and potassium chromate. The solution was prepared 24 hr before
342 use, to allow precipitate formation, and covered with aluminum foil and kept in 37°C. The sample
343 was replaced in a sucrose-based solution (solution C) for 10 min at room temperature. The sections
344 were transferred and agglutinated onto gelatin-coated slides. The sections were rinsed twice for 5
345 min each in distilled water to remove the impregnation solution. The sections were then incubated in
346 the staining solution (Solution D: Solution E: distilled water, 1:1:2) for 10 min at room temperature.

347

348 Analysis of immunohistochemistry.

349 To minimize the anatomical variations of the nose, three coronal sections covered with olfactory
350 neuroepithelium were analyzed every 500 µm intervals. The OE consists of three cell types: olfactory
351 sensory neurons, supporting cells, and basal stem cells. For each OE, coronal sections of the OE
352 were divided into 4 regions: dorsomedial (DM), dorsolateral (DL), ventromedial (VM) and
353 ventrolateral (VL). The thickness of olfactory epithelium was measured between the surface of
354 neuroepithelium and the line of basal cells. We counted the numbers of OMP-positive cells for
355 mature olfactory sensory neurons. To evaluate the numbers of supporting cells (SCs), we defined
356 and counted the SCs as the columnar as the cells located proximal to the nasal cavity, as
357 indicated in a previous report²⁶. To investigate the presence of macrophages in the lamina propria,
358 Iba1-positive cells were counted. All analyses were performed for each group per 100 µm OE length.
359 Three regions were randomly selected, with the regions being at least 100 µm apart, and the
360 averaged values were used. To quantify the densities of the Iba1- and GFAP-positive area, we
361 defined the positive area as one that exceeds two SDs of the mean background intensity.
362 Subsequently, binary images were overlapped onto the original images and the densities were
363 automatically measured using ImageJ software. OMP-positive cells (**Figure 2D**), Iba1-positive areas
364 (**Figure 4D,F,H**), OMP-positive areas (**Figure 3D**), and GFAP-positive areas (**Figure 4-figure**

365 **supplement 1D,F)** were adjusted to normalize the average values in the NQO1-negative. Iba1-
366 positive areas in the hippocampus (**Figure 5E**) were adjusted to normalize the values in the basal
367 region.

368

369 Analysis of Dendritic Spine Density

370 The location of CA1 was identified using a previously published brain map²⁷. Pyramidal neurons in
371 the CA1 were selected and three apical and three basal dendritic segments were analyzed²⁸. For
372 analysis of Golgi-impregnated neurons, the criteria are the following, according to a previous
373 report²⁹: (1) dendrites with a length of at least 50 μ m, (2) consistent and dark impregnation along the
374 entire extent of dendrites, and (3) relative isolation from neighboring impregnated dendrites.

375 Densities of dendritic spines were calculated as the mean numbers of spines per 10 μ m per dendrite
376 per neuron in individual animals per group.

377

378 Microscopy

379 Images (**Figure 5F,G, Figure 1-figure supplement 1A, and Figure 2-figure supplement 1A**) were
380 captured using a digital CCD (Keyence BZ-X800, Japan) with 20 \times (NA = 0.45), 100 \times (NA = 1.45)
381 objective lenses. The size of 20 \times single horizontal images (**Figure 5F, Figure 1-figure supplement**
382 **1A, and Figure 2-figure supplement 1A**) were set to 1920 \times 1440, with pixel size of 0.37 \times 0.37
383 and z-spacing of 5 μ m. The size of 100 \times single horizontal images (**Figure 5G**) were set to 1920 \times
384 1440, with pixel size of 0.07 \times 0.07 and z-spacing of 0.2 μ m. For samples labeled with multiple
385 antibodies (**Figure 1A,B, Figure 2A,B,E,F, Figure 3A,B, Figure 4A,B, Figure 5A,B,C, Figure 1-**
386 **figure supplement 1B,C, Figure 2-figure supplement 1A, Figure 4-figure supplement 1A,B, and**
387 **Figure 5-figure supplement 1A,B**), images were obtained using a confocal microscope (Zeiss LSM
388 880, Germany) with a 20 objective lens (NA = 0.8). Fluorophores were excited by 405, 488, 561 nm

389 lines of diode lasers. The sizes of single horizontal images were set to 512 × 512, with pixel size of
390 0.83 × 0.83 and z-spacing of 1 μm .

391

392 Statistical analysis

393 To prevent arbitrary analysis, all data were randomly and blindly analyzed by two trained human
394 operators. R (<https://www.r-project.org/>) and custom-written Python scripts were used for statistical
395 analysis. Mean \pm SD was used to indicate biological variations. In **Figure 2D, Figure 3D,E, Figure 4D,**
396 **F, H, Figure 5E, Figure 4-figure supplemental 1D, and Figure 4-figure supplemental 1F**, Welch's t-
397 tests were used. Compared to mock groups, comparisons among multiple groups (**Figure 1C, Figure**
398 **2C,G, Figure 3C,E, Figure 5D, Figure 2-figure supplement B,C, Figure 4-figure supplemental C,E,**
399 **and Figure 5-figure supplement 1C,D**) were evaluated with one-way ANOVA and followed by
400 Dunnett's post hoc test. In **Figure 5H**, one-way ANOVA and followed by Tukey's post hoc test were
401 performed. P-values for figures are depicted as follows: * $p < 0.05$, ** $p < 0.01$, *** $p < 0.001$.

402

403 Acknowledgements

404 We would like to thank both the histology core for the HE-staining and imaging core for use of the
405 microscope at UTMB, C.A. Grant, M.A. Micci, K. Suenaga, and H. Iigusa for technical support in
406 preparation of the manuscript, as well as R. Kamei T. Higashi and Y. Kashiwagi for discussions. We
407 also thank T. Makishima for critical reading of the manuscript. This project was funded by John
408 S. Dunn Endowment to S.P.

409

410 Author contributions

411 J.M. designed the study. R.A.R. and J.M. collected the samples. M.K.U. and S.U. designed the
412 experiments and performed the experiments and imaging. M.K.U, S.U., R.K., and K.K. quantified
413 and M.K.U, S.U., and S.H.I. analyzed data. M.K.U, S.U., R.K., K.K., S.H.I., F.I., S.N., T.Y., and S.P.
414 interpreted data. S.U. designed the statistical analysis. S.H.I., F.I., S.N., R.K., T.Y., K.K. and S.P
415 supervised the experiments. M.K.U. and S.U. co-wrote the initial manuscript. S.H.I., F.I., S.N., R.K.,
416 K.K., J.M., R.A.R., T.M., T.Y. and S.P. revised the manuscript. S.P. conceived the study, designed
417 experiments, interpreted data, and co-wrote the manuscript with input from all authors.

418 **Figure supplements legends.**

419 **Figure 1-figure supplement 1** | Distribution of SARS-CoV-2 in the OB.

420 A, Sagittal sections of the whole brain stained by SARS-CoV-2 in mock and 2 dpi. Planes A and B
421 are shown as coronal sections in the Figure B and C. Scale bar, 1 cm.

422 B, Representative image of the coronal section of the OB. Right panels are high-magnification
423 images of the GL in NAD(P)H quinone oxidoreductase 1 (NQO1)-positive (upper) and –negative
424 (lower) regions. White dashed circles indicate glomeruli. Scale bars, 1 mm (left), 100 μ m (right).

425 C, Left panel shows a representative image of the coronal section of the cerebral hemisphere. The
426 white box indicates hippocampal formation (HPF). Right panel is a high-magnification image of the
427 HPF; CA1, CA3, and DG. Scale bar, 1 mm.

428

429 **Figure 2-figure supplement 1** | Cellular properties in the OE due to SARS-CoV-2 infection.

430 A, Representative images of the OE stained with HE and OMP at 5 dpi, 21 dpi, and 42 dpi and
431 mock,. Scale bars, 1 mm (left), 100 μ m (right).

432 B, The thickness of the OE in 4 subdivided areas at 5, 21, and 42 dpi and mock; DM, DL, VM, and
433 DL. (one-way ANOVA followed by Dunnett's post hoc test. *p < 0.05, **p < 0.01, ***p < 0.001).
434 Number of samples; n = 3 (21 dpi) and 4 (5, 42 dpi, and mock).

435 C, Numbers of the OMP-positive cells in the neuroepithelium at 5, 21, and 42 dpi and mock; DM, DL,
436 VM, and DL. (n = 3, one-way ANOVA followed by Dunnett's post hoc test. *p < 0.05, **p < 0.01, ***p
437 < 0.001, † means unevaluable as the OE was completely desquamated and OMP-positive cells were
438 not countable).

439

440 **Figure 4-figure supplement 1 | GFAP-positive cells in the OB.**

441 A, Representative coronal section of the OB stained with glial fibrillary acidic protein (GFAP), NQO1,
442 and Hoechst. Scale bar, 1 mm.

443 B, Representative images of the olfactory nerve layer (ONL), glomerular layer (GL), and external
444 plexiform layer (EPL) stained with GFAP, NQO1, and DAPI. White dashed circles indicate glomeruli.
445 Scale bar, 200 μ m.

446 C,E, Areas of GFAP-positive cells in the ONL and GL. (n = 3, one-way ANOVA followed by
447 Dunnett's post hoc test. **p < 0.01, ***p < 0.001).

448 D,F, Comparison of the normalized values of the density of GFAP-positive cells between NQO1-
449 positive and NQO1-negative regions in the ONL and GL. (n = 3, Welch's t-test).

450

451 **Figure 5-figure supplement 1| Glial activities in the piriform cortex (PC) due to SARS-CoV-2 infection.**

452 A, Representative coronal image of the cerebral hemisphere stained with ionized calcium binding
453 adaptor molecule 1 (Iba1), GFAP, and Hoechst. The white arrow indicates the PC and the white
454 dashed square is a region of interest in the study. Scale bar, 1 mm.

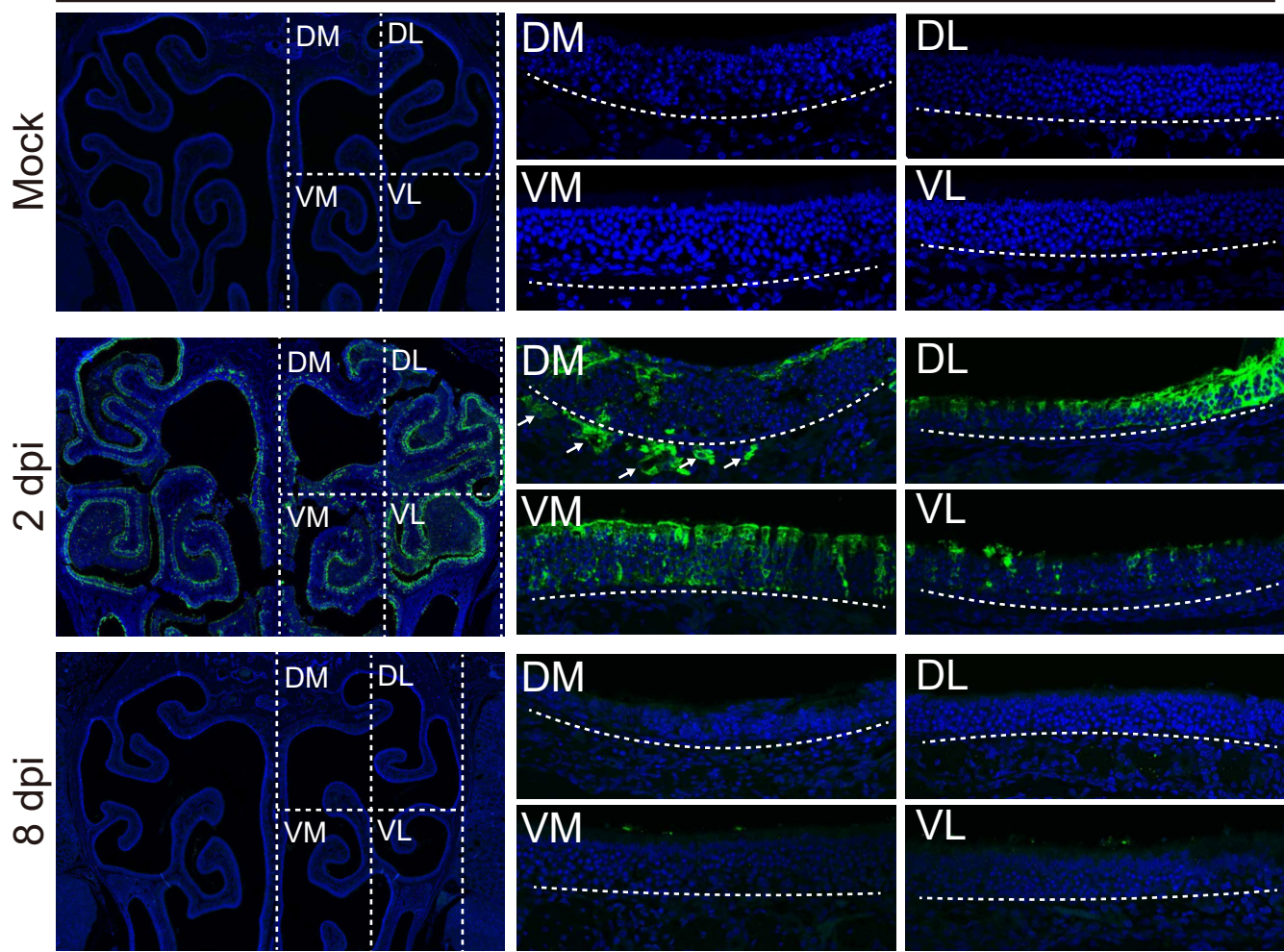
455 B, Representative images of the layers of pia mater, layer 1 (L1), and layer 2 (L2) stained with Iba1,
456 GFAP, and Hoechst at 5, 17, and 42 dpi and mock. White and yellow arrows show Iba1- and GFAP-
457 positive cells, respectively. Scale bar, 100 μ m.

458 C, Quantitative analysis of Iba1-positive cells in the pia mater. (n = 3, one-way ANOVA followed by
459 Dunnett's post hoc test. *p < 0.05, **p < 0.01).

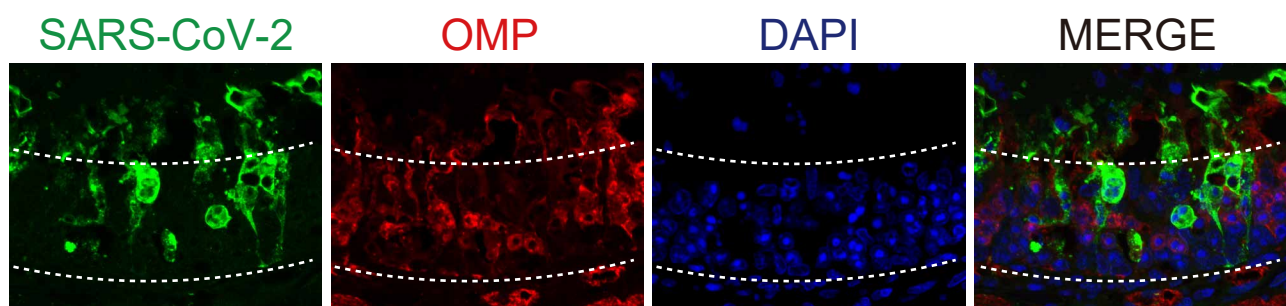
460 D, Iba1-positive densities in L1. (n = 3, one-way ANOVA followed by Dunnett's post hoc test).

A

SARS-CoV-2 DAPI



B



C

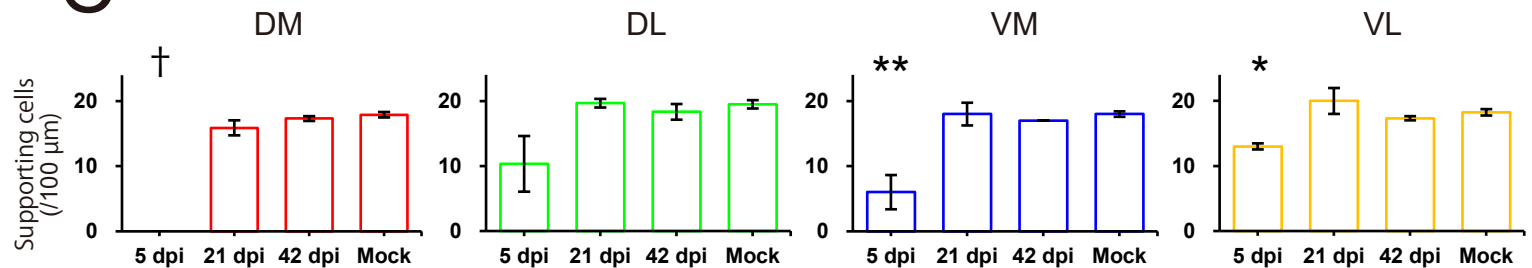


Figure 1

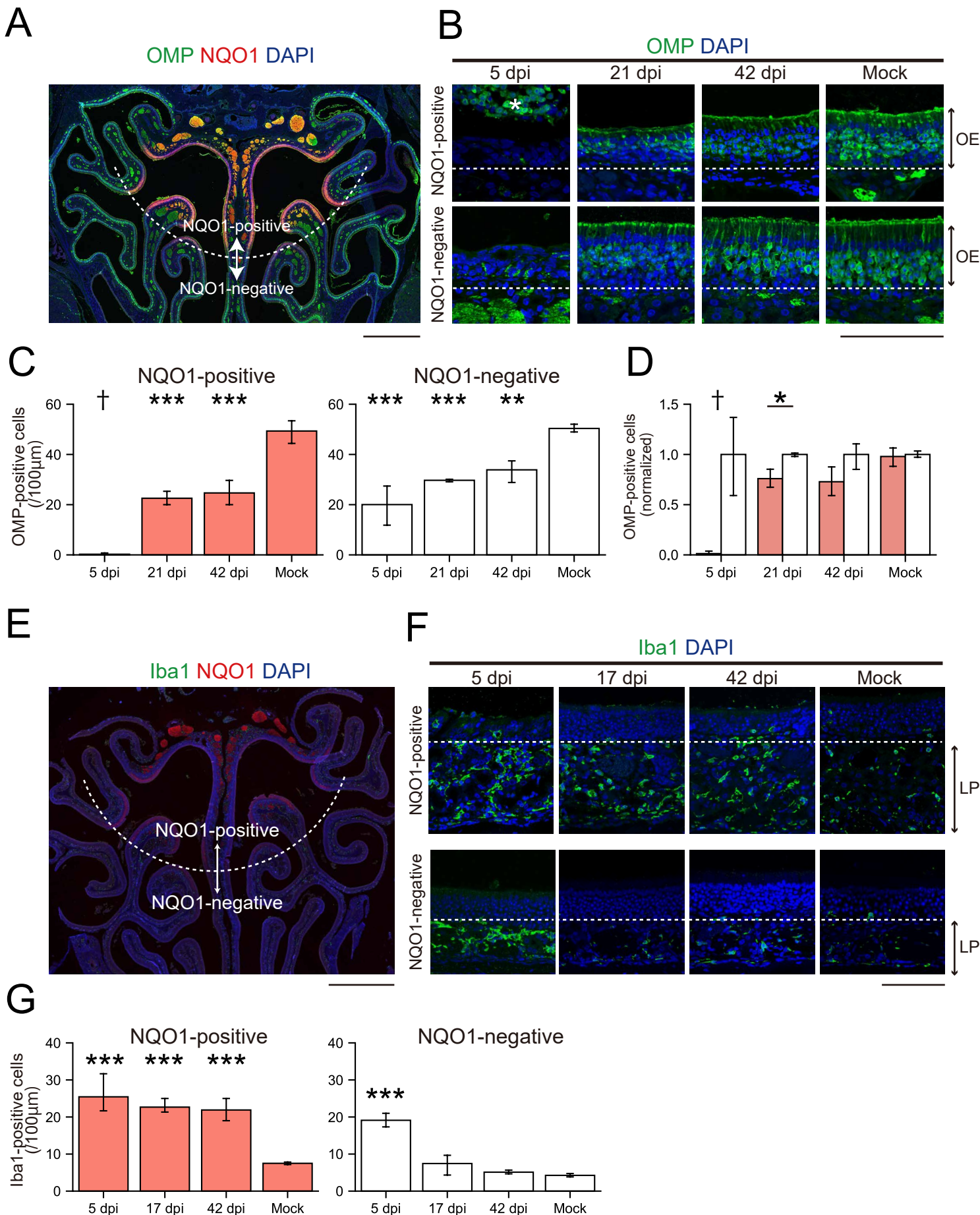
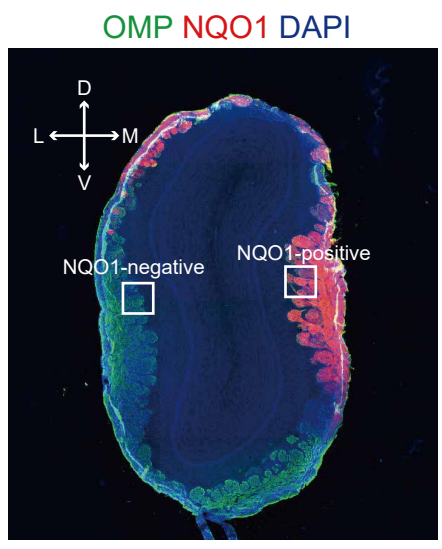
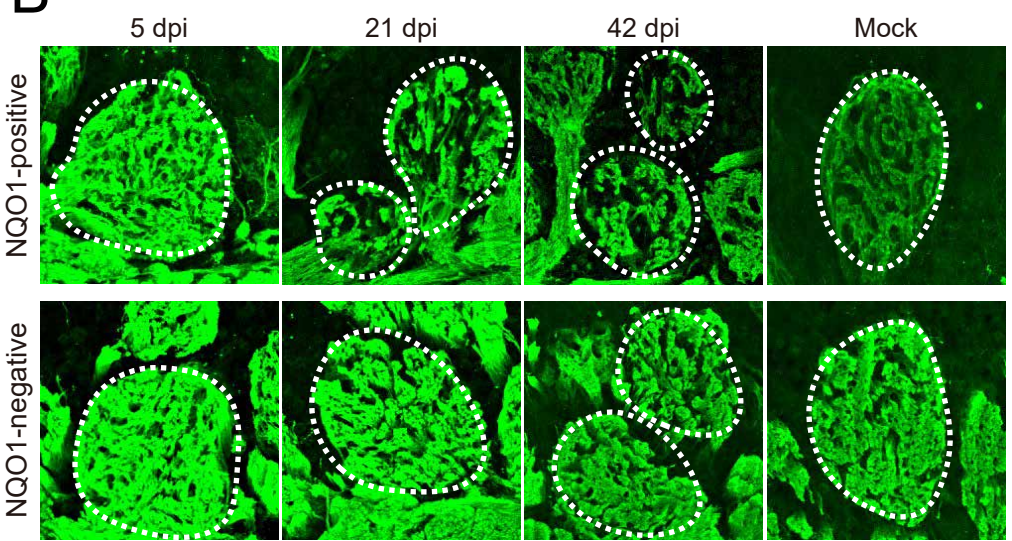


Figure 2

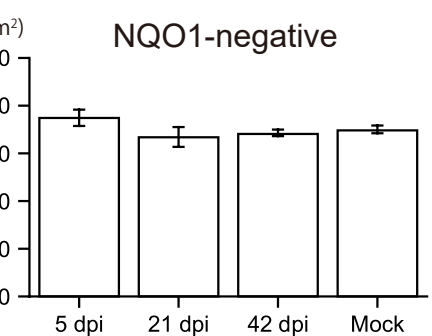
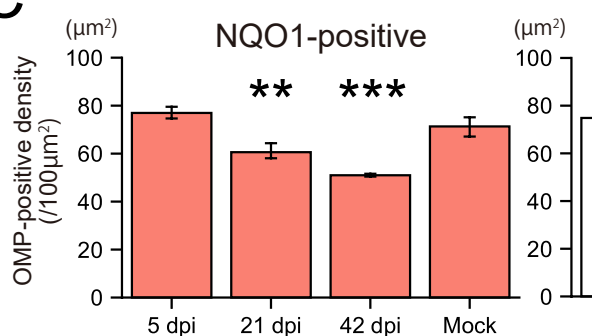
A



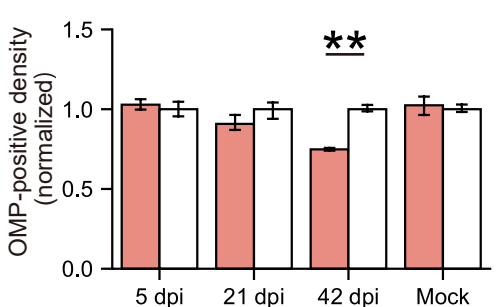
B



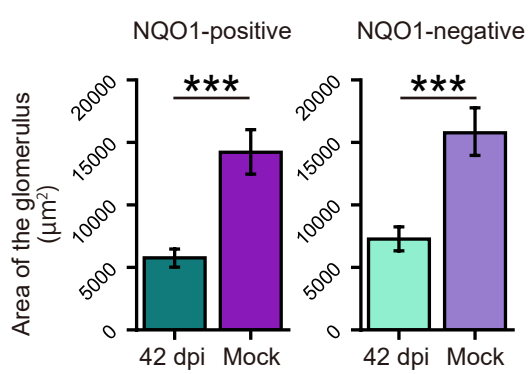
C



D



E



F

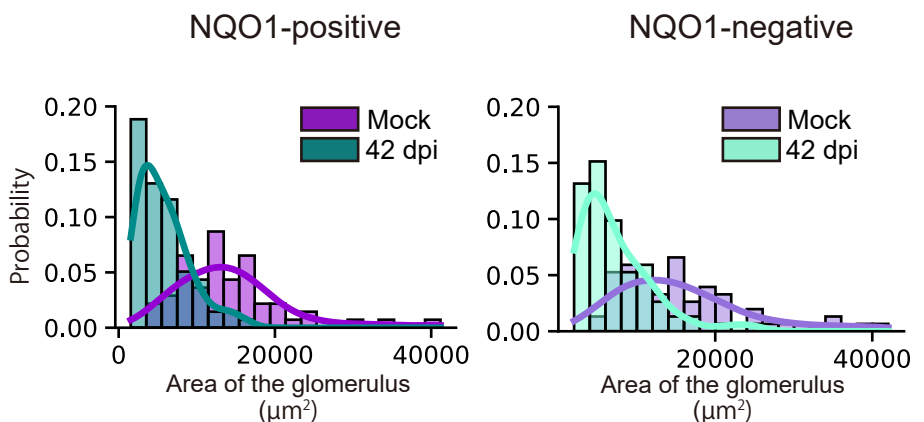
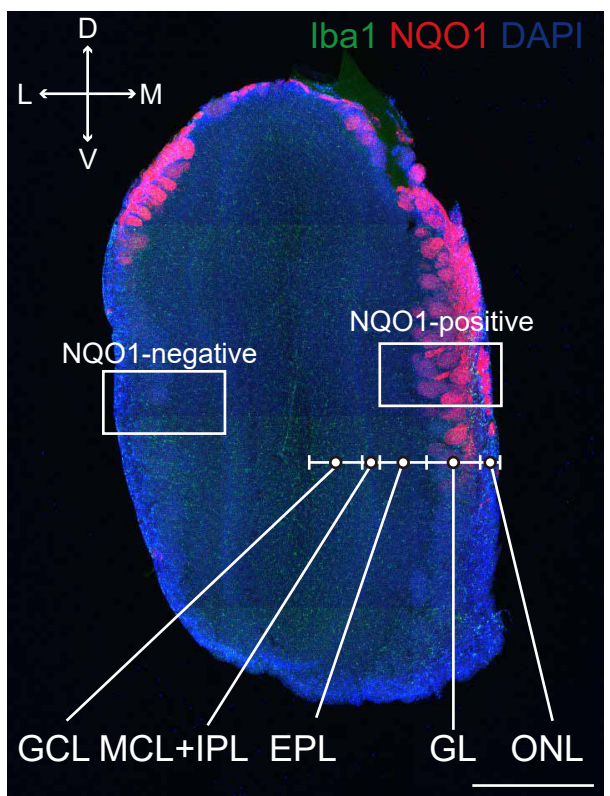
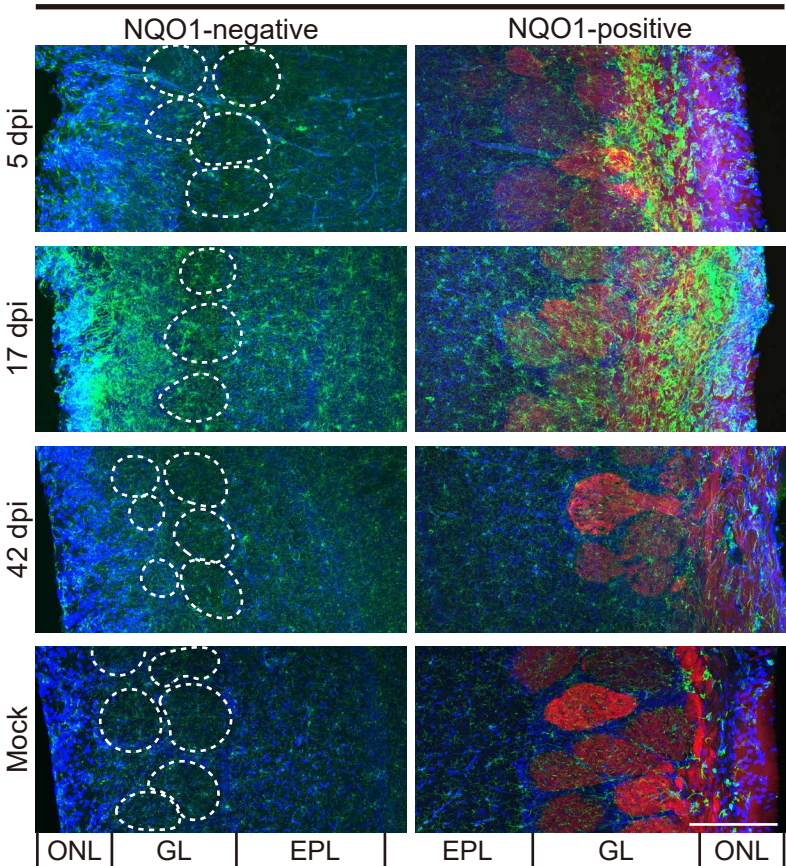


Figure 3

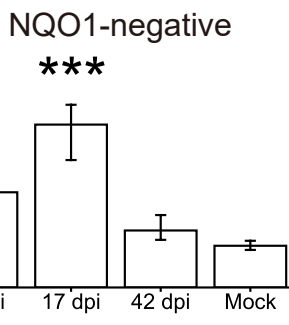
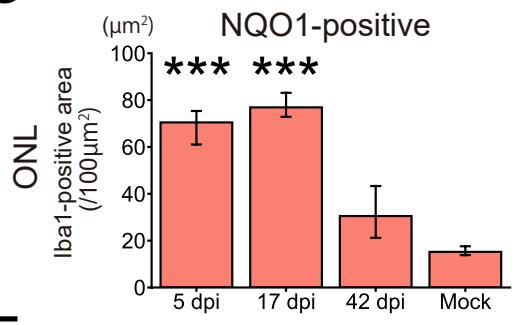
A



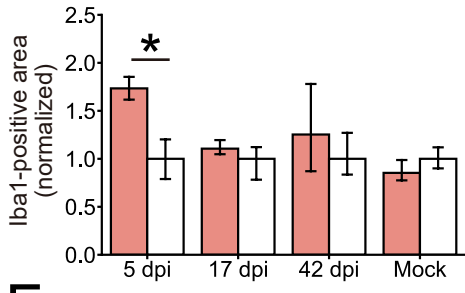
B



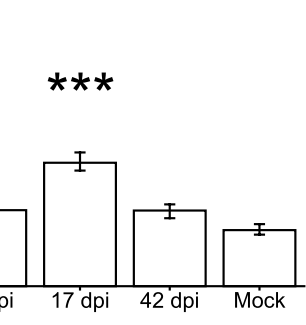
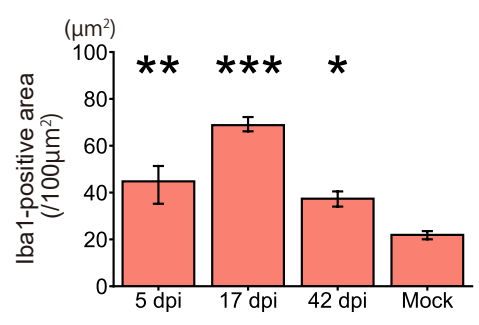
C



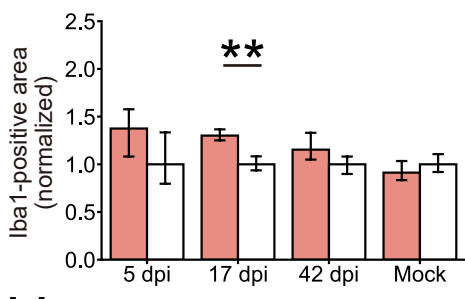
D



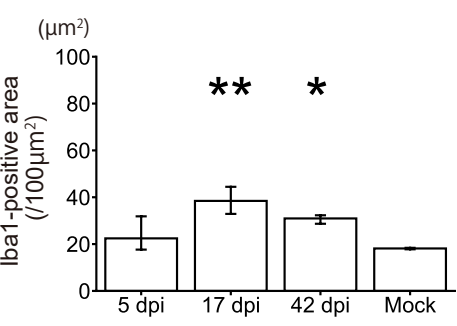
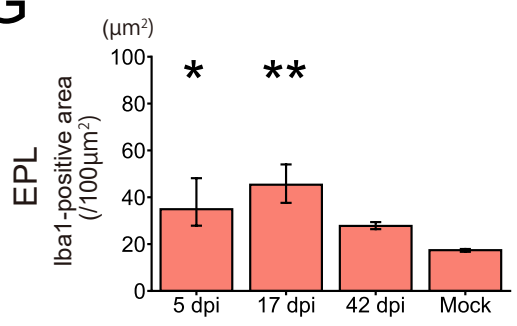
E



F



G



H

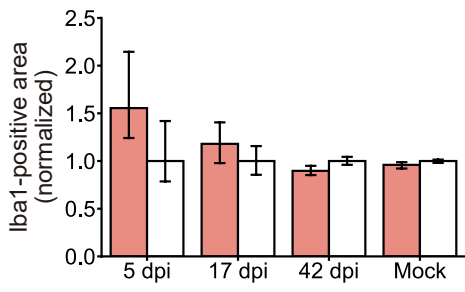
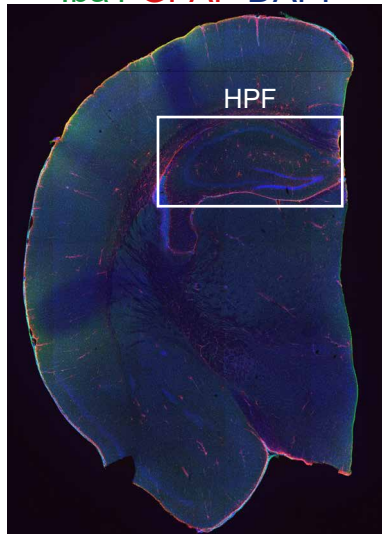


Figure 4

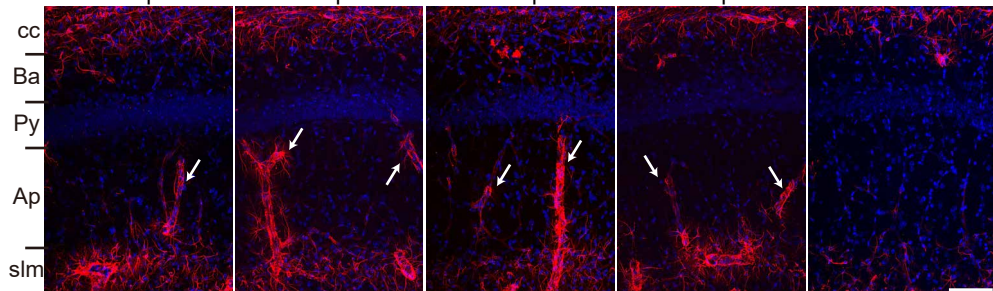
A

Iba1 GFAP DAPI



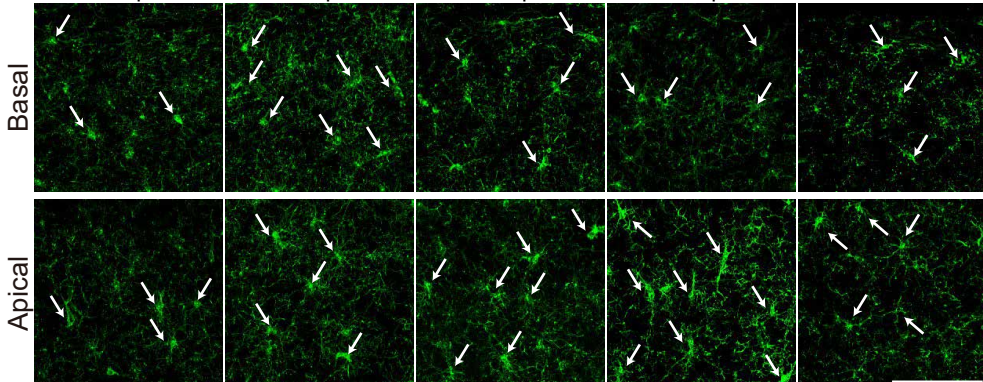
B

5 dpi 8 dpi 17 dpi 42 dpi Mock



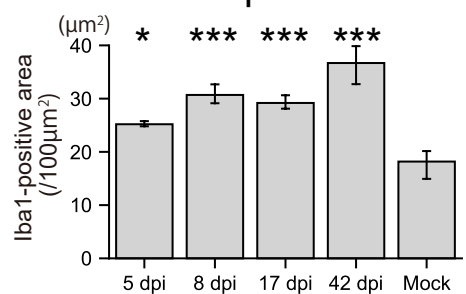
C

5 dpi 8 dpi 17 dpi 42 dpi Mock

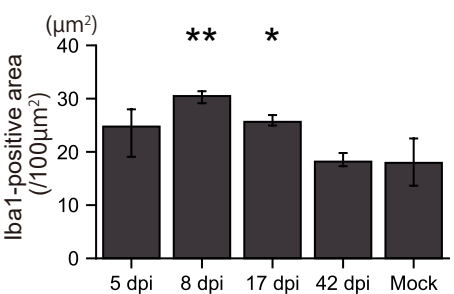


D

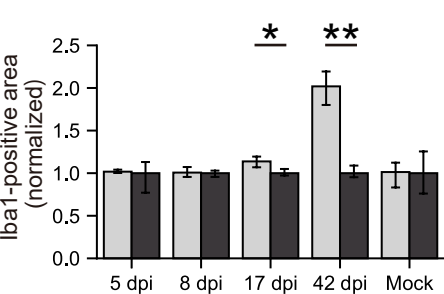
Apical



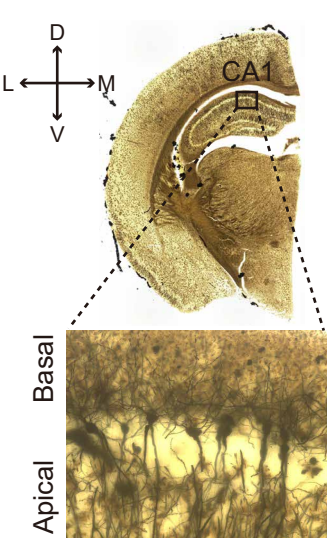
Basal



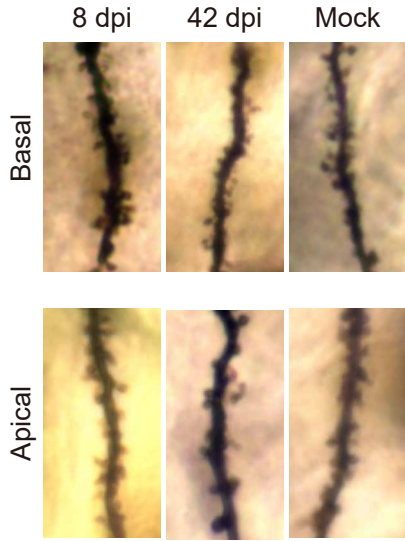
E



F



G



H

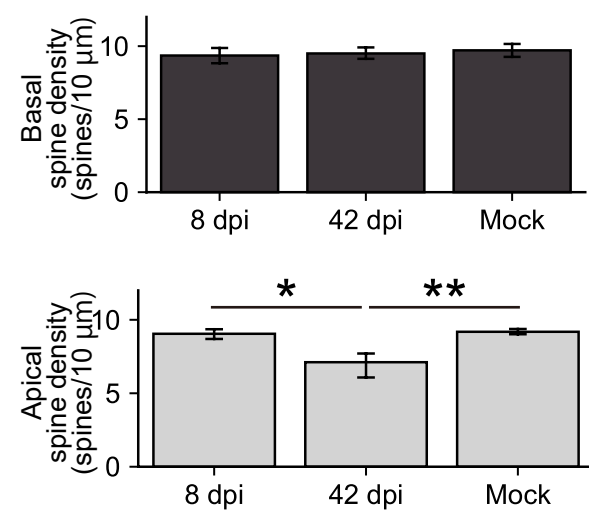


Figure 5

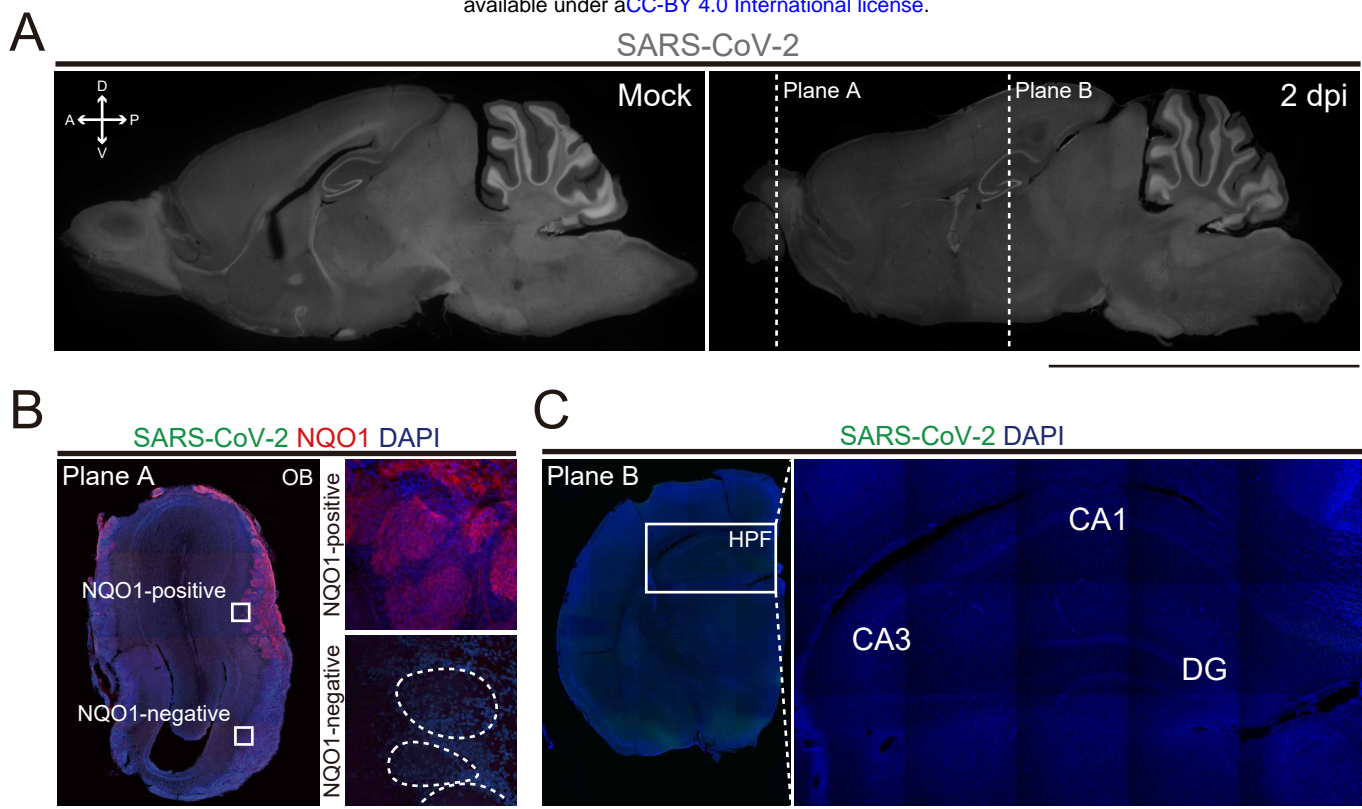
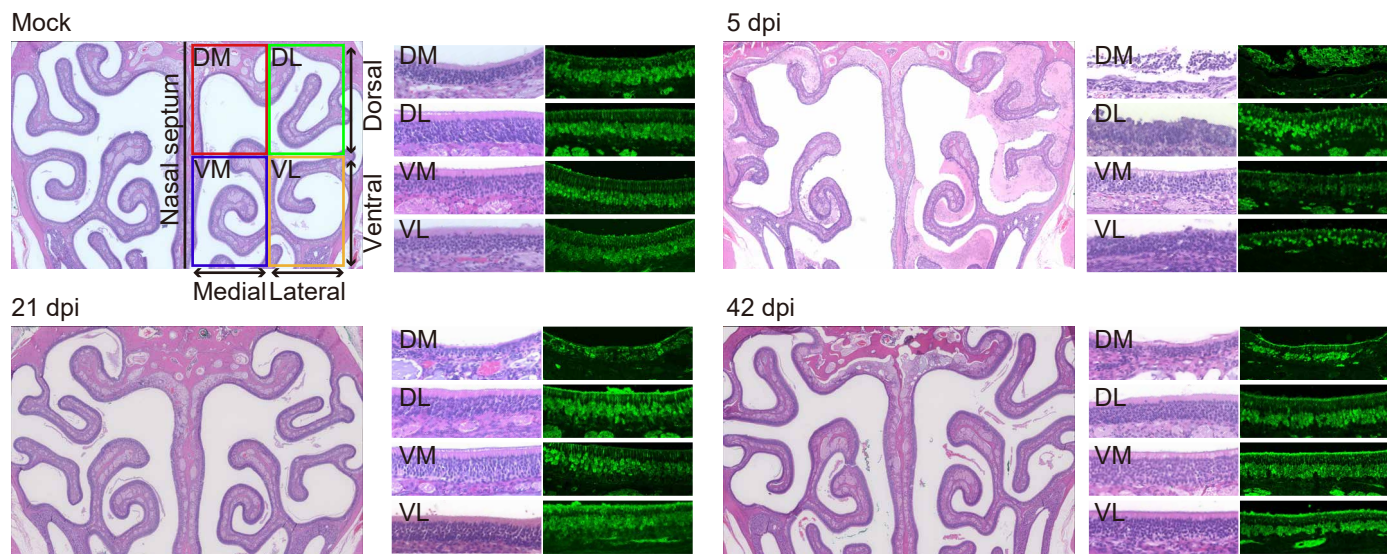
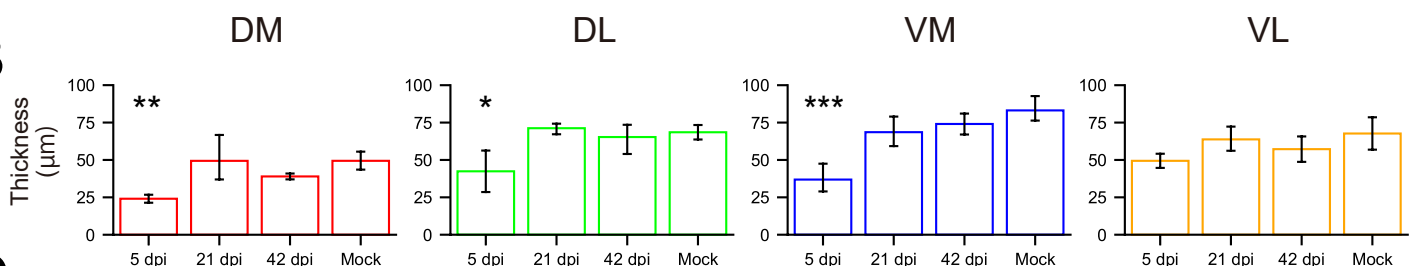


Figure 1-figure supplemental 1

A



B



C

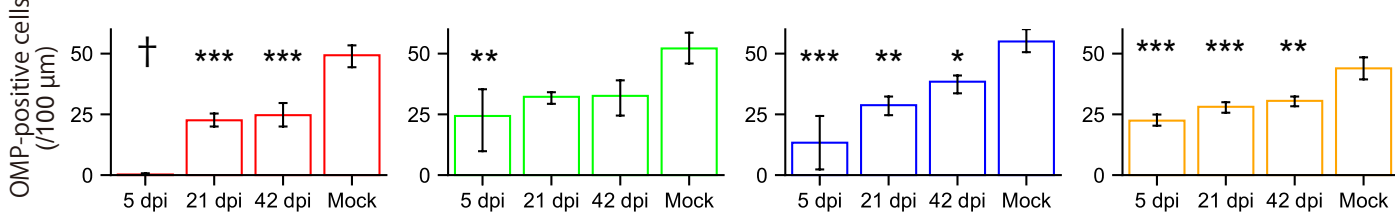
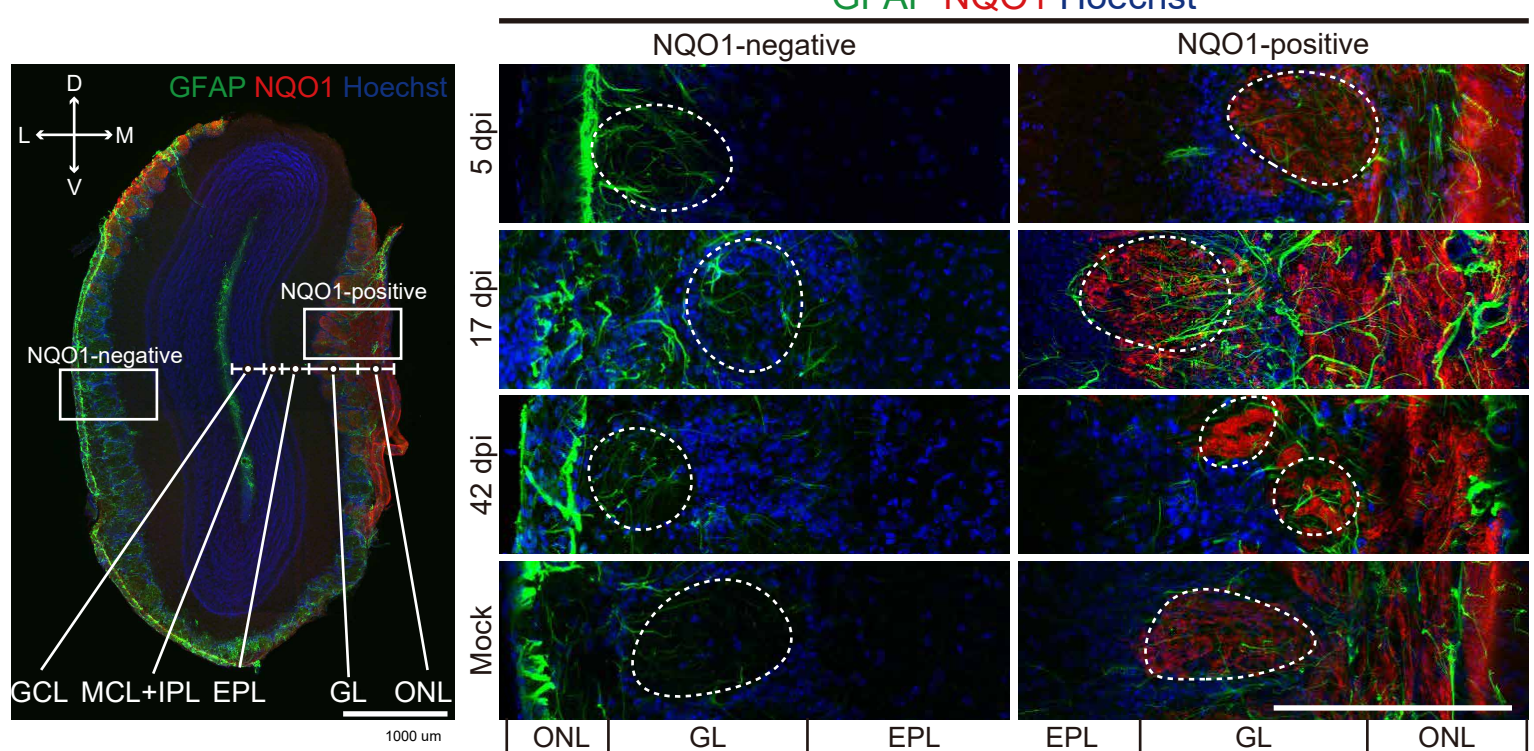
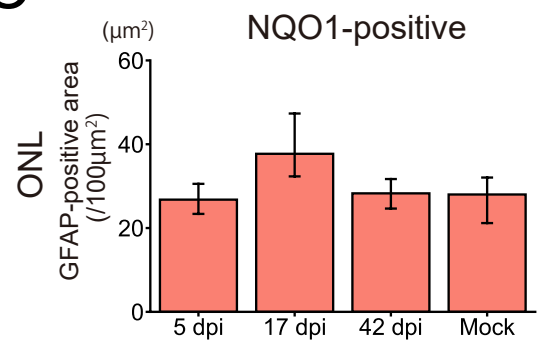


Figure 2-figure supplemental 1

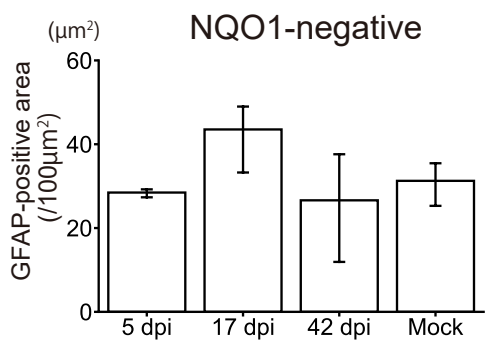
B



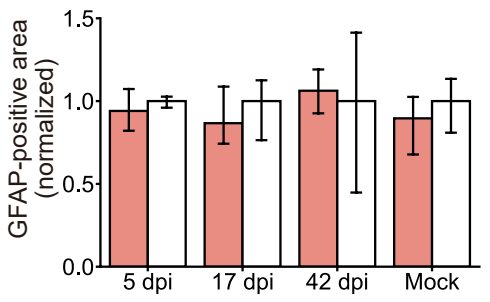
C



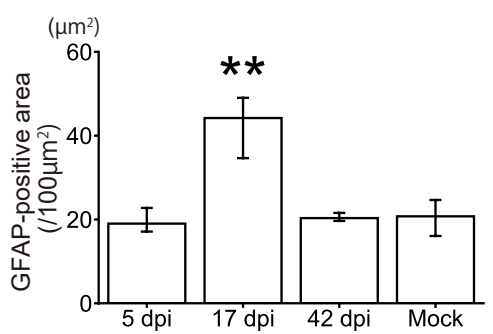
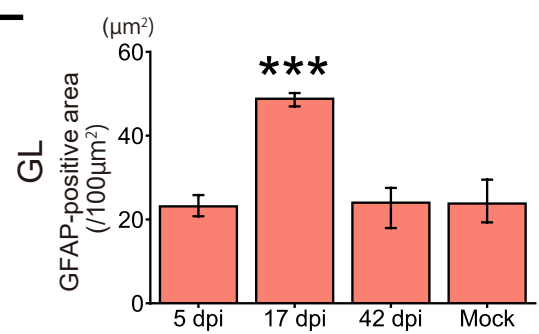
NQO1-negative



D



E



F

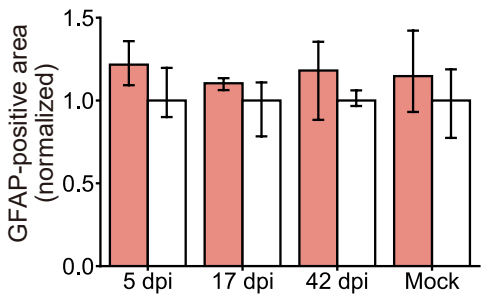
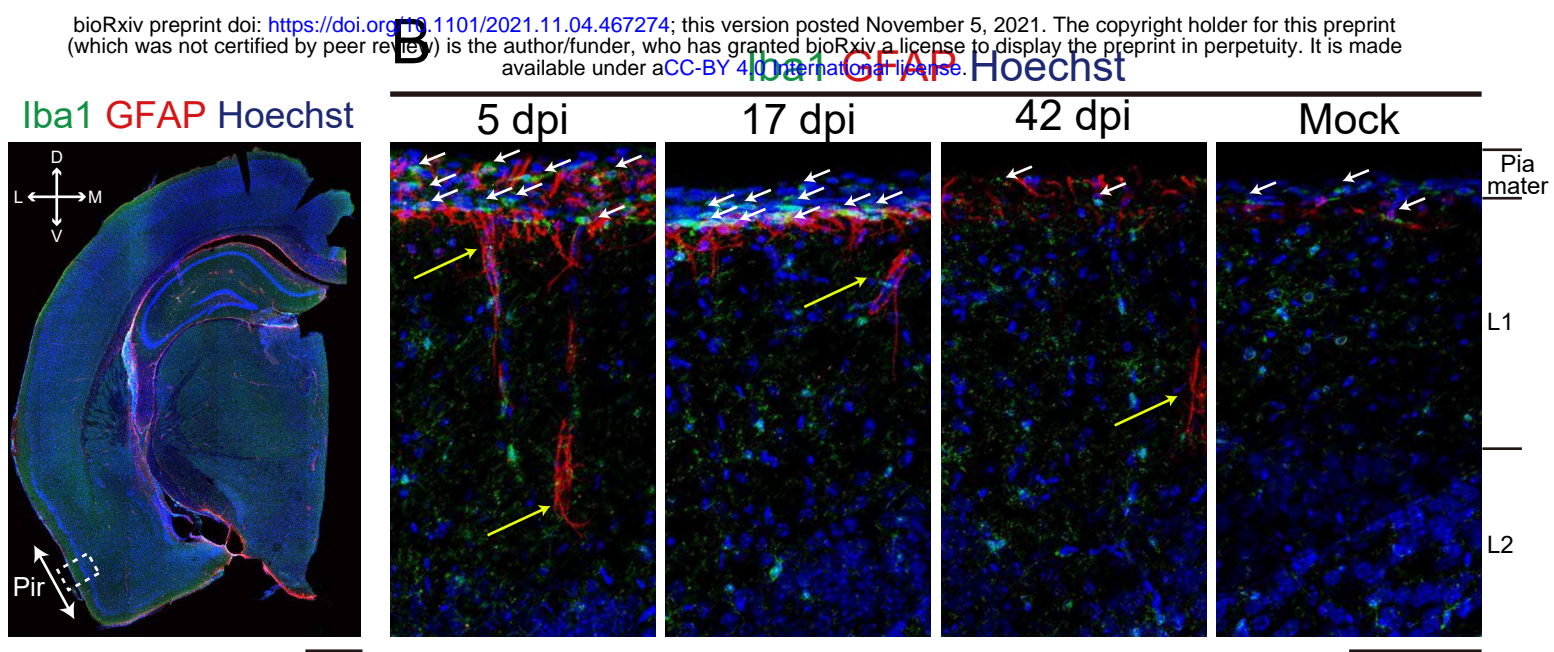
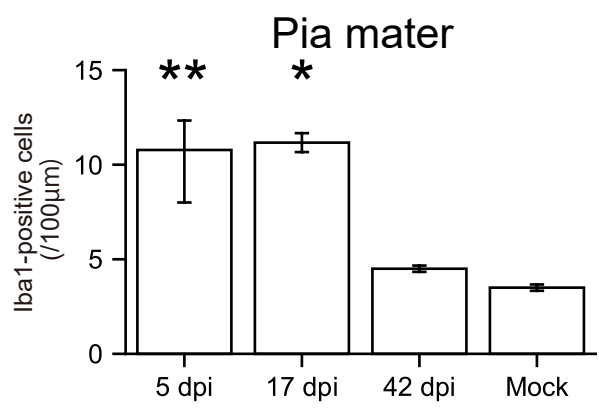


Figure 4-figure supplemental 1

A



C



D

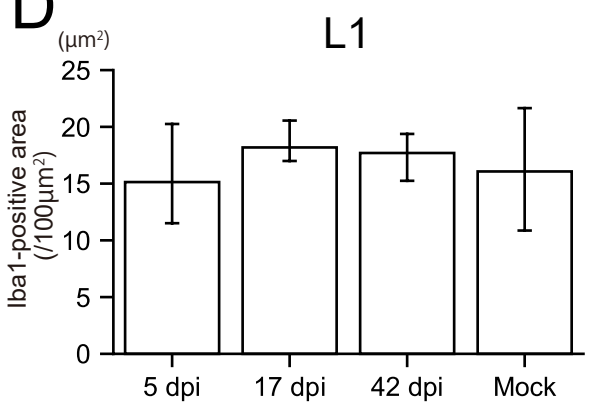


Figure 5-figure supplemental 1